Pore-scale hydro-mechanical modeling of gas transport in coal matrix

Ahmad Mostafa, Luc Scholtès, Fabrice Golfier

Pore-scale hydro-mechanical modeling of gas transport in coal matrix

Ahmad Mostafa[1], Luc Scholtès[2], Fabrice Golfier[1]

[1]Université de Lorraine, CNRS, Laboratoire GeoRessources, Nancy, France

[2]Université Clermont-Auvergne, CNRS, IRD, OPGC, Laboratoire Magmas et Volcans, Clermont-Ferrand, France

Corresponding author email: ahmad.mostafa@univ-lorraine.fr

ABSTRACT:

We present a 3D model coupling a discrete element model and a pore network model specifically developed to describe the different diffusion mechanisms at stake in coal matrix as well as the associated adsorption induced deformations. The material is assumed to be saturated with gas and diffusion occurs through the combination of Knudsen diffusion within the pore space, surface diffusion at the solid surface, and adsorption-desorption at the pore-solid interface. The model is hydro-mechanically coupled in the sense that changes in pore pressure produce hydrostatic forces that deform the solid skeleton, while deformation of the pore space induces pore pressure changes that promote interpore flow. Sorption induced deformations are taken into account by considering an additional pressure term related to the concentration of gas within the medium (the so-called solvation pressure). The implemented transport models are verified against analytical solutions describing diffusion in porous media with and without sorption-desorption, and a comparison is made with a swelling experiment performed on a coal specimen to illustrate the relevance of the proposed approach for describing adsorption induced deformation. As a result, this new pore-scale model offers a precise way to assess coal matrix sorption induced deformation and contributes to the knowledge of CBM storage and transport processes.

Keywords: coal, gas transport, sorption, DEM, PNM, solvation pressure.

1 Introduction

Coalbed methane (CBM), also known as coal seam gas (CSG), has drawn much attention lately as an alternative energy resource. Production curves of CBM reservoirs are very different, however, from the ones of hydrocarbon conventional reservoirs (Liu et al., 2011). As emphasized by several studies (Li et al., 2017; Mostaghimi et al., 2017, 2016; Privalov et al., 2020; Wang et al., 2018), transport and poromechanical properties of coal are strongly driven by topological and morphological features of its pore space.

Coal is fractured by nature; it is a dual porosity/permeability system made up of a porous matrix surrounded by fractures known as cleats (Figure 1, scale II). The orientation of this quasi-orthogonal cleat network including tensile fractures or face cleats, and compressive and strike-slip fractures or butt cleats, depends on the principal stress' directions (Laubach et al., 1998) and provides preferential pathways for fluid flow with fracture apertures up to 100 microns. In contrast, methane gas is stored within the low porosity coal matrix with pore sizes generally varying from a few to several dozens of nanometers (Li et al., 2017; Wang et al., 2018).

The cleat-matrix system compartmentalizes the transport and mechanical properties of coal. Knudsen and surface diffusions prevail in the nanometer-sized pores of the matrix, while molecular diffusion and two-phase Darcy flow occur mainly within the cleat network. All these transport mechanisms induce mechanical couplings related to both (i) the pore pressure changes which may alter the effective stress and consequently impact the bulk volume of the coal and, (ii) the sorption processes which contribute to swell or shrink the coal matrix (Pini et al., 2009; Wang et al., 2011). Indeed, coal can sorb various gases including CO_2, CH_4 and N_2, and the adsorption of these gases induces swelling strains (Ceglarska-Stefańska and Czapliński, 1993; Ceglarska-Stefańska and Zarębska, 2002; Pan and Connell, 2007). The magnitude of adsorption-induced deformation depends on the pores structure as well as on the nature of the gas adsorbed. It is well known for instance that the swelling is much higher with CO_2 than with CH_4 (Brochard et al., 2012), hence advocating the development of enhanced coal bed methane (ECBM) technology combining CBM recovery and CO2 sequestration.

If many experimental studies have attempted to accurately determine this volumetric deformation rate (Majewska et al., 2010) and have given precious insights into the changes in pore size distribution during adsorption/desorption processes, they did not completely succeed to capture the dynamics of mass transfer within the cleat-matrix system since measurements are generally carried out at equilibrium (Wang et al., 2018). Also,

coal measurements are strongly affected by sample preparation, material composition, environment, and methodology (Mostaghimi et al., 2017).

The inherent couplings between the physical processes at stake and the multiscale features of coal need to be explored further to better assess the macroscopic response of the coal matrix and the sorption induced volumetric deformation. If pioneering works (see for instance the review by (Liu et al., 2011)) have focused on permeability models using continuum (Connell, 2016; Guo et al., 2016) or dual-porosity approaches (Bertrand et al., 2017; Ma et al., 2017; Perrier et al., 2018; Wu et al., 2010), much attention has been paid in the last years to study the hydro-mechanical (HM) behavior of coal matrix at the pore-scale. For instance, Liu et al. (Liu and Mostaghimi, 2017) have derived a model based on the lattice Boltzmann method taking into account fluid-rock interactions with permeability and porosity variations to investigate the reactive transport of CO_2-saturated brine in coal fractures. Youjun and Vafai, (Youjun and Vafai, 2017) have simulated fluid flow in pores using a digital SEM image of a coal rock sample. More recently, Sampath et al. (Sampath et al., 2020) have developed a HM model taking into account CO_2 diffusion and adsorption-induced mechanical deformation in coal matrix. To the best of our knowledge, however, a coupled HM model that incorporates the different transport mechanisms combining the diversity of nanoscale processes with the complexity of pore network topology has never been derived for coal matrix.

In this work, we propose a 3D pore-scale model for coal matrix based on a pore network model (PNM) describing gas transport coupled to a discrete element model (DEM) describing the mechanical behavior. The model is based on the framework of the pore scale finite volume (PFV) scheme implemented in the open-source platform YADE DEM (Šmilauer et al., 2015). The DEM-PFV coupled approach was initially designed for upscaling fluid flow in granular materials (Chareyre et al., 2012) and has been afterward used to describe hydro-mechanical processes in both soils (Catalano et al., 2014; Scholtès et al., 2015) and rocks (Papachristos et al., 2017). Lately, Caulk et al. (Caulk et al., 2020) extended its capability by incorporating heat transfer to the scheme and the associated possibility to describe thermo-hydro-mechanical processes. Here, we go further by introducing mass transport and sorption induced deformation processes to its formulation.

In summary, the equations governing the transport and HM schemes are first presented and derived accordingly to the geometric and numerical characteristics of the proposed model. Then, a validation exercise is provided

where each component of the transport model is challenged against analytical solutions of Fick's law considering either pore-pore, pore-particle or particle-particle diffusion mechanisms. Finally, the coupled HM model is used to simulate an experiment from the literature where a coal sample experience swelling due to gas adsorption.

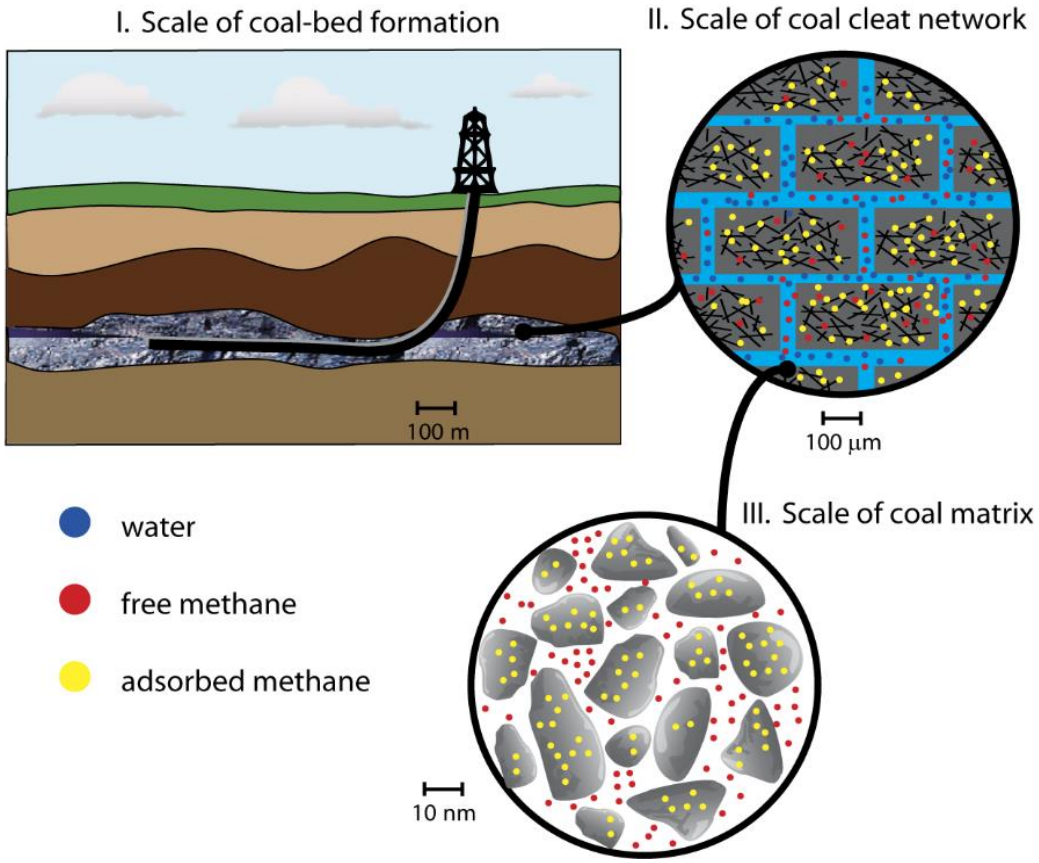

Figure 1 Different scales of a coalbed reservoir.

2 Methodology

The porous coal matrix is modeled based on the assumption that the solid phase is made up of densely packed spherical particles bonded one with another, and the pore space idealized as a network of interconnected pores. The following sections detail the mechanical and transport models, the assumptions made and their respective implementation in YADE DEM.

2.1 Mechanical scheme

The DEM is a numerical method that models geomaterials as assemblies of particles interacting one with another according to predefined contact laws as initially proposed by Cundall and Strack (Cundall and Strack, 1979). Each particle is defined through its own mass, size and position. The numerical scheme relies on an iterative temporal

integration of Newton's second law of motion to describe the movement of each particle depending on the forces they are subjected to. To model coal, we use spherical particles and define elastic-brittle-force displacement laws between the particles, as proposed in the bonded particle model (BPM) introduced by (Scholtès and Donzé, 2013) to simulate rock like materials. The interaction force F between two particles a and b is decomposed into a normal and a shear component.

The normal force is computed as:

$$F_n = k_n \Delta D \tag{1}$$

where ΔD is the relative displacement between a and b, and k_n is the normal stiffness defined by:

$$k_n = E_{eq} \frac{R_a R_b}{R_a + R_b} \tag{2}$$

with E_{eq} an elastic modulus, and R_a and R_b the radii of a and b respectively. In compression, F_n can increase indefinitely. In tension, a maximum acceptable force is defined as a function of the interparticle tensile strength t such as $F_{n,max} = t\ A_{int}$, with $A_{int} = \pi[min(R_a, R_b)]^2$. If $F_n \geq F_{n,max}$, tensile rupture occurs.

The shear force is computed incrementally such as:

$$F_s = \{F_s\}_{updated} + k_s \Delta u_s \tag{3}$$

with k_s the shear stiffness defined as $k_s = P k_n$ with $0 < P < 1$, and Δu_s the relative incremental tangential displacement. F_s can increase up to a threshold value defined by a Mohr-Coulomb type criterion such as $F_{s,max} = c + F_n \tan(\varphi)$, with c the interparticle cohesion, and φ the interparticle friction angle. If $F_s \geq F_{s,max}$, shear rupture occurs.

In addition, the integration of the equations of motion being done through an explicit finite difference scheme, a local non viscous damping is used to dissipate kinetic energy and to ease the convergence of the simulated system toward quasi-static equilibrium (see (Duriez et al., 2016) for details). Basically, the resultant force $\vec{F} = \overrightarrow{F_n} + \overrightarrow{F_s}$ considered in Newton's second law of motion is damped by a force $\overrightarrow{F^d}$ defined as:

$$\overrightarrow{F^d} = -\alpha\ sign\left(\sum \vec{F} . \left(\vec{v} + \frac{\Delta t^m}{2}\vec{a}\right)\right) \sum \vec{F} \tag{4}$$

with α a damping coefficient ($0 < \alpha < 1$), $\vec{v}$ and $\vec{a}$ the velocity and acceleration of the particle respectively, and Δt^m the mechanical time step.

2.2 Mass transport model

The diffusion of gas molecules within coal is rather complex due to the multi-scale architecture of the material, with pore sizes varying over several orders of magnitude (Jing et al., 2017). Theory of gas transport in porous media has a long history from the simple Fick's law for binary systems, to the Stefan-Maxwell equations for multicomponent mixtures and ultimately, the Dusty-Gas Model, based on the Chapman-Enskog kinetic theory and including the couplings between the various mechanisms (Reinecke and Sleep, 2002; Thorstenson and Pollock, 1989). Indeed, different transport modes manifest and drive gas migration in nanoporous media, depending on the pore size and on the flow regime (Do, 1998):

(i) Viscous flow in which displacement of molecules is induced by the mean velocity and governed by the total pressure gradient which acts as driving force.

(ii) Molecular or continuum diffusion where molecular-molecular collision prevails. In the gas mixture, each species moves relative to each other, and the driving force is the molar fraction gradient for an isothermal system.

(iii) Knudsen diffusion in which molecule-wall collisions dominate compared to collisions between molecules. Contrarily to molecular diffusion, each species moves independently from each other. The driving force here is the partial pressure gradient, which reduces to the total pressure gradient for a single species gas flow.

(iv) Surface diffusion in which adsorbed molecules moves along solid surface (pore walls) from one adsorption site to another (Choi et al., 2001).

These different transport mechanisms may compete and combine in a complex way. The relative magnitude of collisions between molecules relative to collisions between molecules and walls (molecular vs Knudsen diffusion) is classically expressed through the dimensionless Knudsen number K_n, defined as the ratio between the molecular mean free path length $\cap$ which is a function of pore pressure, and the mean pore diameter d. For nanoporous material such as coal, and at low pore pressures, $K_n \gg 1$ typically, meaning that Knudsen diffusion generally prevails.

In the present study, we assume that water was previously expelled from coal matrix (residual water is expected to be trapped in the smallest pores that do not participate to flow) so that single-phase gas flow occurs within the pore network. The gaseous mixture is only composed of methane (an ideal gas assumption is employed) and a

part of gas is sorbed on the coal solid phase. Due to the very low permeability of the matrix and considering single-species gas phase, only Knudsen and surface diffusions are thus considered (Figure 2a).

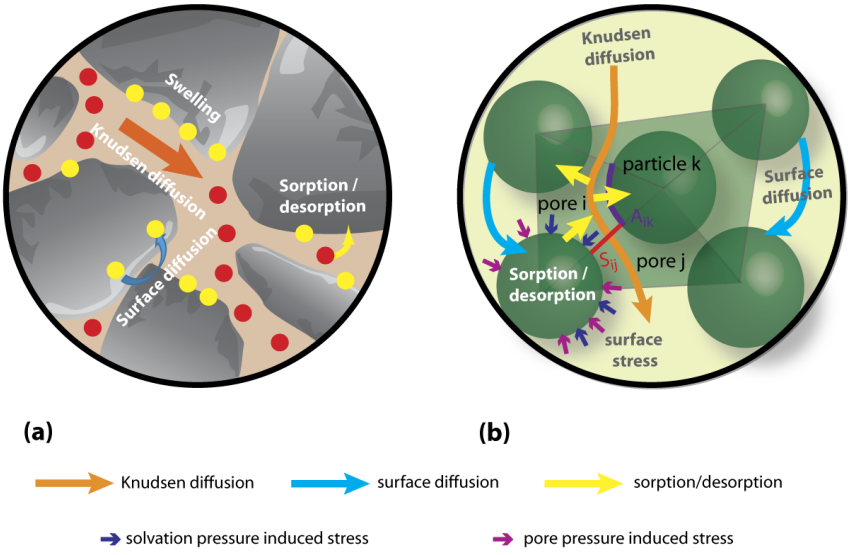

Figure 2 Mass transport and associated diffusion mechanisms in a) coal matrix, b) DEM-PFV model.

The DEM-PFV approach discretizes the pore space of the particle assembly into tetrahedra built from a weighted Delaunay triangulation of the particles' centers (Figure 2b). Each tetrahedron contains both a solid fraction resulting from the intersection between the tetrahedron and the associated vertex spheres, and a fluid fraction (the pore) resulting from the remainder of the tetrahedron volume. Each pore is thus connected to 4 neighboring pores and is in contact with 4 particles through surface areas where mass transport occurs by diffusion.

2.2.1 *Mass balance equation for pores*

Gas molecules are transported from one pore to another and are adsorbed/desorbed from and to the solid particles. Let V_f be the volume of a pore i saturated with fluid (gas). Integrating the continuity equation in pore i gives:

$$\int_{V_f} \frac{\partial c_i}{\partial t} dV + \int_{V_f} \bar{\nabla}.\bar{J}_{pore,i} dV = 0 \quad (5)$$

where c_i is the concentration of gas in pore i, and $\bar{J}_{pore,i}$ represents the gas fluxes coming in and out of pore i. Applying the divergence theorem to Equation (5) gives:

$$\int_{V_f} \frac{\partial c_i}{\partial t}.dV + \int_{\partial V_f} \bar{J}_{pore,i}.\bar{n} dS = 0 \quad (6)$$

Since each pore i is connected to 4 neighboring pores and in contact with 4 particles, the contour surface of each pore can be calculated as:

$$\partial V_f = \sum_{j=1}^{4} \partial V_{pore,i-pore,j} + \sum_{k=1}^{4} \partial V_{pore,i-particle,k} = \sum_{j=1}^{4} S_{ij} + \sum_{k=1}^{4} A_{ik} \quad (7)$$

with S_{ij} and A_{ik} the intersection surface areas between pore i and pore j, and between pore i and particle k respectively.

In our modeling approach, Knudsen diffusion describes the pore-pore diffusion fluxes and adsorption/desorption describes the pore-particle diffusion fluxes (Figure 2). Equation (7) can then be written as follows:

$$\int_{Vf} \frac{\partial c_i}{\partial t} dV = -\sum_{j=1}^{4} \int_{S_{ij}} \bar{J}_{ij}^{K}.\bar{n}dS - \sum_{k=1}^{4} \int_{A_{ik}} \bar{J}_{ik}^{ad}.\bar{n}dS \quad (8)$$

where $\bar{J}_{ij}^{K}$ is the Knudsen diffusion flux between pore i and pore j, and $\bar{J}_{ik}^{ad}$ is the adsorption/desorption flux between pore i and particle k.

2.2.1.1 Knudsen diffusion

For a single-species phase flow along a straight circular capillary tube, the Knudsen diffusion flux can be defined as (Do, 1998):

$$\bar{J}^{K} = -D^{K}\bar{\nabla}c \quad (9)$$

$$\bar{J}^{K} = -D^{K}\frac{1}{RT}\bar{\nabla}p$$

with $p = cRT$ the gas pressure, R the gas constant (j/mol/k) and T the absolute temperature (K). The Knudsen diffusion coefficient D^{K} (m^2/s) is given by:

$$D^{K} = \frac{2r}{3}\sqrt{\frac{8RT}{\pi M_g}} \quad (10)$$

with r the pore hydraulic radius, and M_g the molar mass (kg/m^3).

The Knudsen flux may thus be written in terms of concentration between pore i and pore j such as:

$$\overline{J_{ij}^{K}} = -\frac{2r}{3}\sqrt{\frac{8RT}{\pi M_g}}\,\bar{\nabla}c_{ij} \quad (11)$$

with r computed as proposed by (Chareyre et al., 2012) in the PFV scheme. Then the spatial integration of Equation (11) between pores i and j gives:

$$\int_{S_{ij}} \bar{J}_{ij}^{K}.\bar{n}dS = -\frac{S_{ij}}{L_{ij}}\frac{2r}{3}\sqrt{\frac{8RT}{\pi M_g}}\left(c_j^t - c_i^t\right) \quad (12)$$

where L_{ij} is the distance between the centers of pore i and pore j.

2.2.1.2 Sorption

Sorption generally refers to the transport and attachment of a solute to the surface of a solid phase. Sorption processes are usually investigated at equilibrium through isotherms that relate the amount of adsorbed solute to the bulk concentration at constant temperature. In our modeling approach, we define kinetics formulations balancing the relative rates of adsorption and desorption (Raoof et al., 2012).

- **Linear first order sorption**

Linear sorption is characterized by an infinite number of sites on the particles' surfaces. As a result, solid particles can adsorb an infinite number of gas molecules according to the following relation:

$$\frac{\partial s}{\partial t} = (K_{att}c - K_{det}s) \quad (13)$$

where s $(\mathrm{mol/m^3})$ is the amount of solute adsorbed onto the solid phase surface, c $(\mathrm{mol/m^3})$ is the concentration of solute in the mobile phase (gas), K_{att} and K_{det} are respectively the adsorption and desorption coefficients defining the rate of adsorption/desorption, and t is the time (s). At equilibrium we recover the linear relationship:

$$K_d = \frac{K_{att}}{K_{det}}.$$

$$\text{where } \frac{\partial s}{\partial t} = 0 \text{ then } s = \frac{K_{att}}{K_{det}}c = K_d.c \quad (14)$$

- **Langmuir sorption**

If adsorption is limited by the number of sites on the solid surface (Liu et al., 2019), the following nonlinear relation can be used:

$$\frac{\partial s}{\partial t} = \frac{s}{s_{max}}K_{det} - \left(1 - \frac{s}{s_{max}}\right)K_{att}c \quad (15)$$

where the sorption is proportional to the number of available sites $(1 - \frac{s}{s_{max}})$, s_{max} being the maximum amount of sorbed concentration. At equilibrium, we recover:

$$\frac{\partial s}{\partial t} = 0, \text{then } \frac{s}{s_{max}} = \frac{K_d.c}{1+K_d c} \quad (16)$$

In our model, the diffusion fluxes between pores and particles can thus be described either by the linear relation of Equation (13) or by the nonlinear relation (Langmuir isotherm) of Equation (15). For instance, the spatial integration of the pore-particle diffusion flux between pore *i* and particle *k* in the case where it is governed by the Langmuir isotherm is defined as:

$$\int_{A_{ik}} \bar{j}_{ik}^{ad}.\bar{n}dS = \frac{A_{ik}}{A_k}\left[K_{det}\frac{s_k^t}{s_{k,max}} - \left(1 - \frac{s_k^t}{s_{k,max}}\right)K_{att}c_i\right] \times V_p \quad (17)$$

where s_k (mol/m^3) is the solute concentration adsorbed on the surface of particle k, A_k is the overall surface of particle k, and V_p is the volume of particle k.

Finally, considering both sorption Equation (17) and Knudsen diffusion Equation (12), the evolution of each pore concentration is obtained by an explicit integration over time such as:

$$c_i^{t+\Delta t} = \sum_{i=1}^{4}\frac{V_p A_{ik}}{V_f A_k}\left[\left(1 - \frac{s_k^t}{s_{k,max}}\right)K_{att}c_i^t - K_{det}\frac{s_k^t}{s_{k,max}}\right]\Delta t^{\frac{ad}{des}} + \sum_{i=1}^{4}\frac{S_{ij}}{V_f L_{ij}}\ \frac{2r}{3}\sqrt{\frac{8RT}{\pi M_g}}\left(c_j^t - c_i^t\right)\Delta t^K + c_i^t \quad (18)$$

with $\Delta t^{\frac{ad}{des}}$ and Δt^K the associated time steps.

2.2.2 *Mass balance equation for particles*

The amount of gas molecules adsorbed on the solid particles results from the transport of gas molecules both from neighboring solid particles and from pores (Figure 2b). Particle-particle flux occurs by surface diffusion, while pore-particle flux results from adsorption/desorption process. Let V_p be the volume of a particle k. Integrating the mass balance equation on particle *k* gives:

$$\int_{V_p}\frac{\partial s_k}{\partial t}dV + \int_{V_p}\bar{\nabla}.\bar{J}_{particle,k}\ dV\ = 0 \quad (19)$$

where s_k is the adsorbed concentration on particle *k*, and $\bar{J}_{particle,k}$ represents the gas fluxes coming in and out of particle *k*.

Applying the divergence theorem to Equation (19) gives:

$$\int_{V_p} \frac{\partial s_k}{\partial t} dV + \int_{\partial V_p} \bar{J}_{particle,k} . \bar{n} dS = 0 \quad (20)$$

Since each particle is connected to N particles (N depends on the spatial arrangement of the particles within the medium), and to 4 pores, the contour surface of each particle can be calculated as:

$$\partial V_p = \sum_{l=1}^{N} \partial V_{particle,k-particle,l} + \sum_{i=1}^{4} \partial V_{particle,k-pore,i} = \sum_{l=1}^{N} S_{kl} + \sum_{i=1}^{4} A_{ik} \quad (21)$$

where S_{kl} is the intersection surface area between particle k and particle l, and A_{ki} is the intersection surface area between particle k and pore i (Figure 2b).

Equation (21) can then be written as follows:

$$\int_{V_p} \frac{\partial s_k}{\partial t} dV = -\sum_{l=1}^{N} \int_{S_{kl}} \bar{J}_{kl}^{S} . \bar{n} dS - \sum_{i=1}^{4} \int_{A_{kl}} \bar{J}_{ki}^{ad} \bar{n} . dS \quad (22)$$

where $\bar{J}_{kl}^{S}$ is the surface diffusion flux between particle k and particle l, and $\bar{J}_{ki}^{ad}$ is the adsorption/desorption flux between particle k and pore i.

2.2.2.1 Surface diffusion

Particle-particle flux is governed by surface diffusion in which gas molecules are transported from the surface of a grain to the surface of a neighboring grain. In essence, molecules jump from an adsorption site to another adsorption site. The diffusive flux is thus driven by the gradient of sorbed concentration between and within particles and the surface diffusion flux can be expressed as:

$$\bar{J}^{s} = -D^{S} \bar{\nabla} s \quad (23)$$

The surface diffusion coefficient D^S is known to be a function of temperature following the Arrhenius equation and strongly depends on the surface loading (Do, 1998). For sake of simplicity, however, it will be kept constant hereafter.

The spatial integration of the diffusive flux between particles k and l is defined as:

$$\int_{S_{kl}} \bar{J}_{kl}^{S} . \bar{n} dS = -\theta \frac{D^S S_{kl}}{L_{kl}} (s_k^t - s_l^t) \quad (24)$$

where S_{kl} is the intersection surface area between particle k and particle l computed here as $S_{kl} = 4 r_l r_k$, L_{kl} is the distance between the centers of particle k and particle l, r_l and r_k are the radiuses of particle k and particle l,

and θ is a scaling parameter enabling to constrain the transport properties of the simulated medium depending on the structural characteristics of the particle assembly (θ is related to the particle connectivity which is a function of the particle size distribution of the packing as well of its porosity).

2.2.2.2 Sorption

Particle-pore diffusion processes are governed by the same mechanisms than pore-particle diffusion processes (see Equation (17)).

Finally, combining both sorption Equation (17) and surface diffusion Equation (24), the evolution of each particle concentration is obtained by an explicit integration over time such as:

$$s_k^{t+\Delta t} = \sum_{i=1}^{4} \frac{A_{ik}}{A_k} \left[\left(1 - \frac{s_k^t}{s_{k,max}} \right) K_{att} c_i^t - K_{det} \frac{s_k^t}{s_{k,max}} \right] \Delta t^{\frac{ad}{des}} + \sum_{l=1}^{m} \theta \frac{D^S S_{kl}}{V_p L_{kl}} (s_k^t - s_l^t) \Delta t^{sd} + s_k^t \quad (25)$$

with $\Delta t^{\frac{ad}{des}}$ and Δt^{sd} the associated time steps.

2.3 Hydro-mechanical coupling

The hydraulic forces acting on a solid particle immersed in a fluid result from both the pressure and viscous stress acting on its surface (Chareyre et al., 2012). In coal matrix with nanometer pores, pore velocities are very low (they are actually neglected in the mass transport model) and hence are the viscous stress forces. We thus only consider the contribution of the normal pressure forces which result from pressure losses within the pore space as follows:

$$\overrightarrow{F_{ij}^k} = A_{ij}^k (p_i - p_j) \overrightarrow{n_{ij}} \quad (26)$$

where $p_i - p_j$ represents the pressure difference between pore i and pore j, A_{ij}^k is the intersection surface area between particle k and the pore throat between pore i and pore j, $\overrightarrow{n_{ij}}$ is the unit vector pointing from pore i to pore j. As shown in (Catalano et al., 2014) and in (Scholtès et al., 2015), the HM coupling resulting from Equation (26) enables the DEM-PFV model to simulate conventional poromechanical behaviors as described by Biot's theory (Biot, 1941).

The classical Biot's theory states that the mechanical behavior of a porous medium depends on the bulk fluid pressure only (p_f) without considering its detailed composition. This means that two pore fluids with different compositions having the same bulk pressure should produce the same volumetric deformation. This is not verified

for swelling materials like coal which shows different deformation amplitudes depending on the nature of the pore fluid (Ottiger et al., 2008). It is now well known that the deformation of coal is not solely governed by the pore bulk pressure: as for all swelling materials, sorption processes induce additional deformation related to the nature of the sorbed molecules (Brochard et al., 2012). Gas molecules get adsorbed at the surface of the pores and induces a surface excess free energy. An additional interfacial force is thus exerted and resulting stress develops within the porous medium. Different approaches were proposed to introduce these nanoscale features into an extended poromechanical equation to explain the sorption-induced deformations from a continuum description. First works have introduced the so-called solvation pressure to describe swelling since in confined pores, pressure is not anymore a scalar (Gor and Neimark, 2010; Kowalczyk et al., 2008; Ustinov and Do, 2006; Yang et al., 2010). A second class of models, based on an energy balance approach, r relates the changes in surface potential energy due to gas adsorption to the elastic energy ("Dilatation of Porous Glass - SCHERER - 1986 - Journal of the American Ceramic Society - Wiley Online Library," n.d.; Dolino et al., 1996; Grosman and Ortega, 2008; Pan and Connell, 2007). Other researchers also have reformulated the poroelastic constitutive equations by introducing an apparent porosity and an interaction free energy that are both related to the Gibbs adsorption isotherm (Mushrif and Rey, 2009; Perrier et al., 2018; Pijaudier-Cabot et al., 2011; Sampath et al., 2020; Vermorel and Pijaudier-Cabot, 2014). In contrast, Vandamme and co-workers (Brochard et al., 2012; Espinoza et al., 2014, 2013; Nikoosokhan et al., 2014) have made use of the bulk pressure and of the swelling strain to express the sorbed amount or the adsorption-induced pressure.

In the present work, the sorption-induced deformations are interpreted in terms of the solvation pressure or adsorption pressure p_s, that is related to the amount of gas molecules attached to the solid skeleton. Specifically, the total pore pressure in each pore i is equal to the sum of the bulk fluid pressure p_f and of the solvation pressure p_s such as:

$$p_i = p_{i,f} + p_{i,s} \tag{27}$$

with $p_{i,f}$ and $p_{i,s}$ defined as follows:

$$p_{i,s} = \sum_{k=1}^{4} \frac{A_{i,k} \times p_s^k}{A_{i,k}} \quad (28)$$

$$p_{i,f} = c_i RT \quad (29)$$

where the solvation pressure related to the amount of gas molecules attached to the particle k is denoted p_s^k and computed as

$$p_s^k = \alpha s_k RT \quad (30)$$

A_{ik} is the intersection surface area between particle k and pore i, and α is a coupling coefficient. Hereafter, α is fixed constant but it is not necessarily the case (Brochard et al., 2012).

Although the solvation pressure is dependent of the adsorbed amount on a grain and hence should be specific to a given particle, it is also a pressure which is summed up with the bulk pressure specific to a pore. To further explain how this additional pressure term is calculated within the pore space, we illustrate in Figure 3 the different situations that can be encountered:

- Case 1: for connected pores (belonging to the connected porosity which will be further discussed in Section 3), we compute a contact surface weighted average solvation pressure for each particle in contact with pore i, and the fluid pressure value depends on the gas pressure gradient within the percolating pore space.
- Case 2: for isolated pores (belonging to the unconnected porosity), the fluid pressure and the solvation pressure are fixed to zero resulting in a zero-total pore pressure. These pores also have no contribution on the fluxes related to the surrounding pores and particles.

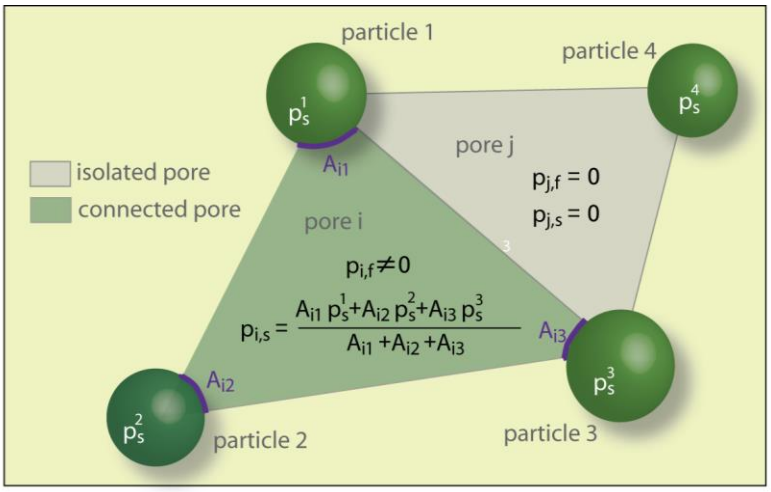

Figure 3 2D representation of pore pressure distribution within the pores of the DEM-PFV model: distinction between connected pores and unconnected pores

3 Model implementation

3.1 Scaling strategy

If the interparticle properties presented in Section 2.1 can be calibrated so that the emergent mechanical properties of the DEM model match those of the material to model (see (Scholtès and Donzé, 2013) for details of the procedure), the diffusion mechanisms at stake require some adjustments of the transport model. For instance, coal matrix has a porosity that is significantly smaller than the porosity of an assembly of spherical particles. Basically, the pore space of the model is scaled so that the effective volume of fluid is $V_{f,eff}$ equal to:

$$V_{f,eff} = V_f \frac{n_m}{n_a} \tag{31}$$

with n_a the porosity of the spherical particle assembly, and n_m the porosity of the actual material.

Scaling the diffusive fluxes is actually sufficient to match the required porosity without changing the volume of both the pore space and the solid phase in the discretized equations, resulting in a total mass balance that accurately represents the material to model as follows:

For particles: $$\bar{J}_{eff} = \bar{J}\frac{1-n_a}{1-n_m} \quad (32)$$

For cells: $$\bar{J}_{eff} = \bar{J}\frac{n_a}{n_m} \quad (33)$$

with $\bar{J}$ the non-scaled flux calculated according to the previous sections and $\bar{J}_{eff}$ the effective ("scaled") diffusive flux.

In addition, we also introduced a procedure to adjust the poromechanical response of our DEM-PFV model since the Biot coefficient of a DEM assembly is intrinsically equal to 1 given the rigid particle assumption of the DEM formulation. As a matter of fact, according to the poroelasticity theory (Detournay and Cheng, 1993), the contribution of the pore pressure p to the overall deformation of porous media is defined through the effective stress such as

$$\sigma' = \sigma - bp \quad (34)$$

where σ' is the effective stress, σ is the total stress, and b is the Biot coefficient equal to $1 - \frac{K}{K_s}$ with K the bulk modulus of the medium, and K_s the bulk modulus of the solid phase. This effective stress produces volumetric strain ε_v which, for a swelling material, presents an additional term of adsorption induced strain ε_s as follows:

$$\varepsilon_v = -\frac{1}{K}\left(\sigma - bp_f\right) + \varepsilon_s \quad (35)$$

where $\sigma = \frac{\sigma_{kk}}{3}$ is the mean stress and ε_s is defined such as:

$$\varepsilon_s = b\frac{p_s}{K} \quad (36)$$

Instead of applying a global scaling factor to Equation (27), we introduced the possibility to neutralize a certain amount of pores within the pore network so that the connected porosity of the particle assembly $n_{a,c}$ is equal to:

$$n_{a,c} = bn_a \quad (37)$$

with b directly equal to the Biot coefficient of the material. The neutralized pores (unconnected porosity) correspond to tetrahedra randomly chosen within the triangulated mesh where gas transport calculations are simply not performed. These isolated pores thus participate to the overall deformability of the particle assembly

due to their compliance without contributing to its poromechanical response as illustrated in Figure 4.

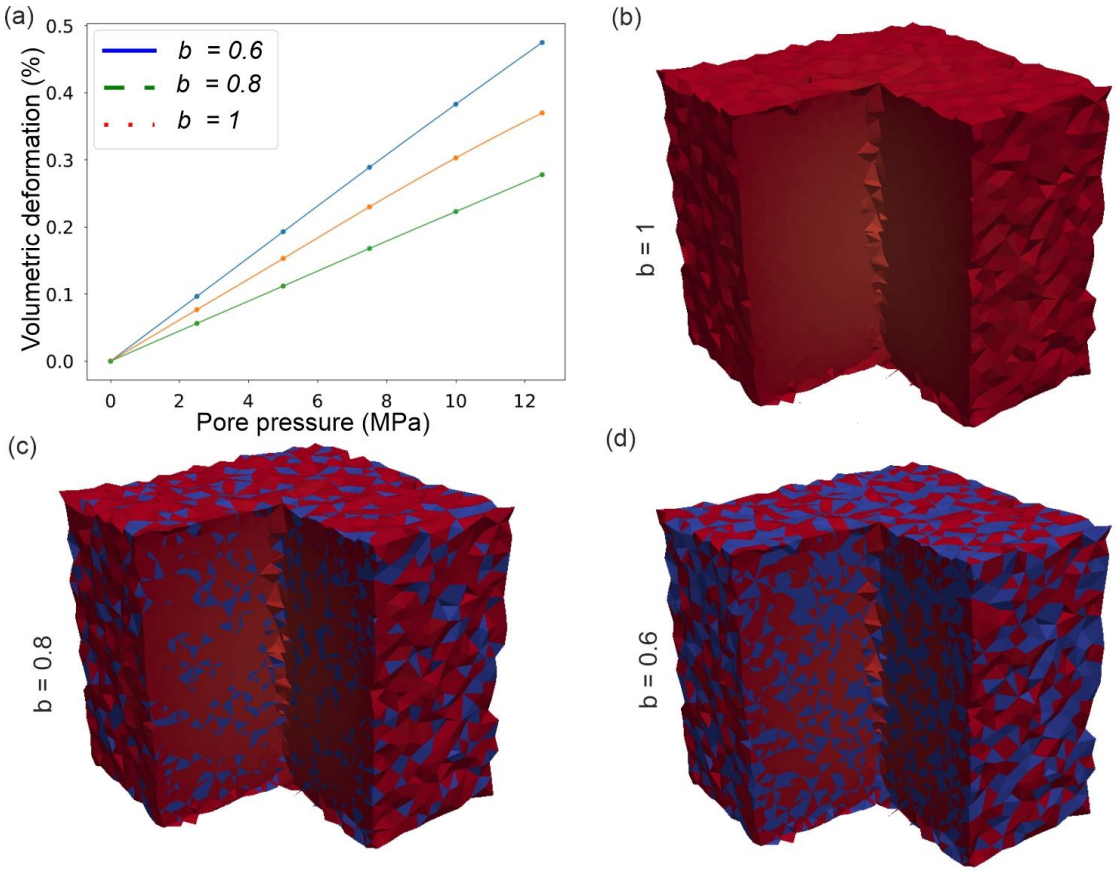

Figure 4 Illustration of the connected porosity $n_{a\mathcal{L}}$ and of its effect on the Biot coefficient, Equation (37): a) Volumetric deformation as a function of pore pressure increase and b,c,d) pressure distribution at equilibrium (p_{CO2}=12.5 MPa) in numerical samples with different pre-defined Biot coefficients (the connected pores are in red and the isolated pores in blue).

3.2 Numerical stability

Numerical stability needs to be considered in every explicit numerical scheme as any effect can only move by a maximum of one spatial grid block in one time step. For instance, in the general case of a 2D diffusion problem, the explicit discretization reads:

$$\frac{u_i^{t+\Delta t}-u_i^t}{\Delta t} = D\,\frac{u_{i+1}^t-2u_i^t+u_{i-1}^t}{\Delta x^2} \tag{38}$$

where D is the diffusion coefficient. Solving Equation (38) for $u_i^{t+\Delta t}$ leads to:

$$u_i^{t+\Delta t} = r u_{i+1}^t + (1-2r)\, u_i^t + r u_{i-1}^t \quad (39)$$

with $r = D\frac{\Delta t}{\Delta x^2}$ the Fourier Number. Applying the Von Neumann stability analysis, the FTCS (Forward Time Centered Space) method is satisfied only if the following condition is fulfilled:

$$r \leq \frac{1}{2} \text{ then } \Delta t \ \leq \frac{\Delta x^2}{2D} \quad (40)$$

In our model, in addition to the mechanical time step that governs the solid particles motion, three-time steps exist due to the three different types of transport mechanisms occurring respectively between pore-pore, pore-particle and particle-particle. To ensure the stability of the numerical scheme, the simulation time step Δt is set up equal to a fraction of the minimum time step $\Delta t_{min} = \min\left(\Delta t^m, \Delta t^K, \Delta t^{\frac{ad}{des}}, \Delta t^{sd}\right)$ required to ensure the stability of the numerical scheme (in all our simulations, the time step was defined equal to $0.8\,\Delta t_{min}$).

4 Verification of the transport models

To verify the correct implementation of the transport equations in our DEM-PFV model, we compared its predictions to analytical solutions of Fick's law considering different 1D problems. For that purpose, we built up a pseudo 1D numerical assembly with dimensions equal to L_0 x $0.2L_0$ x $0.2L_0$ m, made up of 1,000 particles with radii varying between 7.1 and 13 mm, and 5,500 cells. In all the verification examples presented below, HM couplings were not considered, and the simulated medium was non deformable (the mechanical scheme was turned off and the particles fixed in space and time). In the present section and for the sake of comparison, all results and variables will be presented dimensionless. The *x*-coordinate, the Knudsen diffusion coefficient D^K and the concentration *c* are normalized respectively by the sample length L_0, the gas diffusion coefficient D_0 and the inlet concentration c_0. The dimensionless time is defined as $t = Dt_0/L^2$ where t_0 is the physical time. Similar normalization holds for the sorbed concentration *s* and the surface diffusion coefficient D^s. The different test cases with the corresponding parameter values used in the simulations and analytical solutions are gathered in Table 1.

Table 1.

Numerical parameters of the different verification test cases.

Parameter	Test case 1	Test case 2	Test case 3
n	0.45	0.47	0.45
Dimensionless time step Δt	9e-7	9e-6	9e-7
D^K/D_0	1	-	1
D^S/D_0	-	1	-
θ	-	1.12	-
$K_d = k_{att}/k_{det}$	-	-	2
k_{att}	-	-	0.116
k_{det}	-	-	0.058

4.1 *Test case 1: Knudsen diffusion*

First, we consider diffusion of non-sorbing species within a nanoporous material. As a consequence, only Knudsen diffusion occurs, and both sorption and surface diffusion may be neglected. The boundary value problem is thus defined by the following initial and boundary conditions:

$$\frac{\partial c}{\partial t} = D^K \frac{\delta^2 c}{\partial x^2}, \quad \forall x \in [0, L_0] \tag{41}$$

$$c(x,0) = c_0, \quad \forall x \in [0, L_0]$$
$$c(0,t) = c(L_0,t) = 0$$

Using Fourier series, the unsteady solution of this 1D diffusion problem can be written as follows:

$$c(x,t) = \sum_{m=1}^{\infty} \frac{2}{\pi}\left(\frac{1-cos(m\pi)}{m}\right) sin\left(m\pi \frac{x}{L_0}\right) e^{-\frac{D^K}{n_a L_0^2}(m\pi)^2 t_0} \tag{42}$$

The numerical assembly, illustrated in Figure 5a, was subjected to the initial and boundary conditions defined in Equation (41) and the simulation was run with the parameters presented in Table 1.

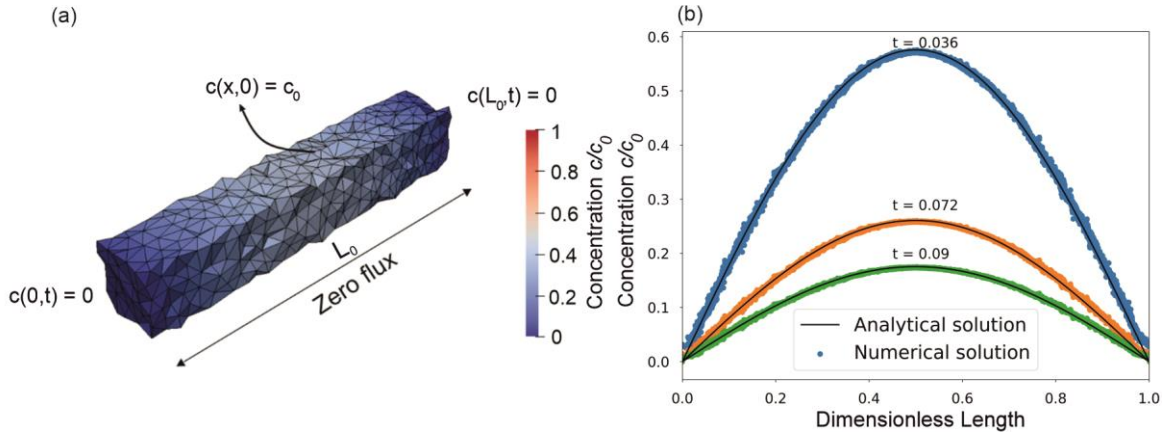

Figure 5 a) Concentration distribution in pores at t=0.04. b) Numerical and analytical concentration profiles in pores at different times.

As shown in Figure 5b, the concentration distribution in the numerical model matches perfectly the analytical solution in space and time, confirming the accuracy of the numerical scheme for simulating Knudsen diffusion.

4.2 Test case 2: surface diffusion

The second test case assumes that the gaseous species is now irreversibly adsorbed and may only diffuse through the solid grains. Surface diffusion is thus considered as the only effective transport mechanism and the problem is defined by the following initial and boundary conditions:

$$\frac{\partial s}{\partial t} = D^S \frac{\delta^2 s}{\partial x^2}, \quad \forall x \in [0, L_0]$$

$$s(x,0) = s_0, \quad \forall x \in [0, L_0] \tag{43}$$

$$s(0,t) = s(L_0,t) = 0$$

This 1D diffusion problem is very similar to the first one and the analytical solution in terms of Fourier series can be written as follows:

$$s(x,t) = \sum_{m=1}^{\infty} \frac{2}{\pi}\left(\frac{1-cos(m\pi)}{m}\right) sin\left(m\pi \frac{x}{L_0}\right) e^{-\left(\frac{D^S}{(1-n_a)L_0^2}\right)(m\pi)^2 t_0} \tag{44}$$

The numerical values used in the simulation are presented in Table 1. The parameter θ was initially calibrated since the number of contacts between particles depends on the packing characteristics (samples are generated using a random packing procedure, considering a pre-defined size distribution). Figure 6a displays an example of the concentration field in the solid grains at a given time of the simulation, while a comparison of the numerical solutions with averaged concentration profiles at different times is provided in Figure 6b. As for test case 1, the concentration distribution in the numerical model matches perfectly the analytical solution in space and time, showing the correctness and reliability of our surface diffusion model and of its implementation.

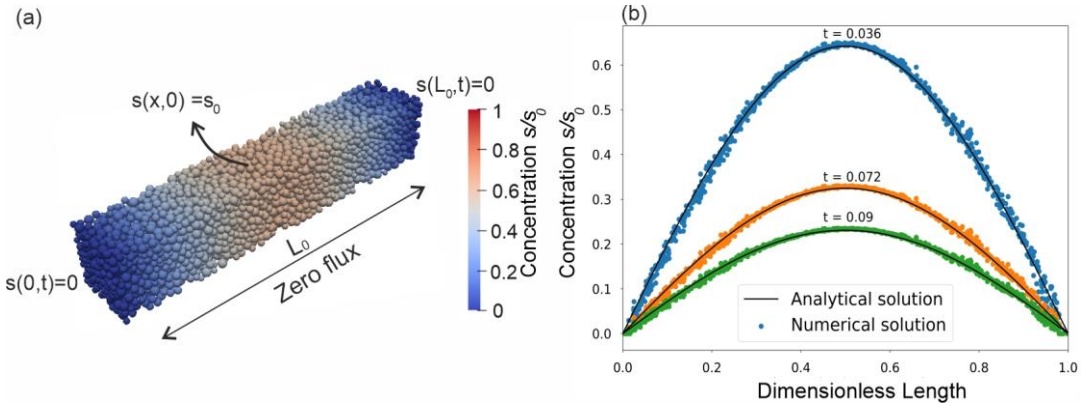

Figure 6 Concentration distribution in particles at t = 0.04. b) Comparison of numerical and analytical concentration profiles in particles at different times.

4.3 Test case 3: Knudsen diffusion with adsorption/desorption

For this test case, we consider diffusion of a sorbing species within a non-swelling porous material. Here, we used a linear isotherm to describe the solute adsorption onto the solid grains (see Section 2.2.1.2) and surface diffusion is neglected (no transport within the solid phase). The system is initially at thermodynamic equilibrium so that partitioning between gas and solid phases is respected. The adsorption and desorption kinetics coefficients K_{att} and K_{det} are chosen high enough so that the equilibrium state is verified at each time step. Based on these assumptions, the 1D boundary value problem is defined as follows:

$$\frac{\partial c}{\partial t} = D^K \frac{\delta^2 c}{\partial x^2}, \quad \forall x \in [0, L_0]$$

$$s(x,t) = K_d\, c(x,t), \quad \forall x \in [0, L_0] \tag{45}$$

$$c(x,0) = c_0\,; s(x,0) = K_d c_0, \quad \forall x \in [0, L_0]$$

$$c(0,t) = c(L_0,t) = 0$$

and the transient analytical solution is given by:

$$c(x,t) = \sum_{m=1}^{\infty} \frac{2}{\pi}\left(\frac{1-cos(m\pi)}{m}\right) sin\left(m\pi \frac{x}{L}\right) e^{-\left(\frac{D^K}{n_a(1+K_d)L_0^2}\right)(m\pi)^2 t_0} \tag{46}$$

The numerical parameters used for this test case are presented in Table 1.Figure 7a displays an example of the concentration fields in both pores and grains obtained at a given time while a comparison of the numerical solutions with averaged concentration profiles at different times is provided in Figure 7b. Here again, a very good

agreement between the numerical and analytical solutions is obtained. We may also observe that our kinetics formulation converges well to the equilibrium since the partitioning between gas and solid grains, driven by $K_d = 2$, is always respected. This comparison validates the coupling method between diffusion and sorption processes.

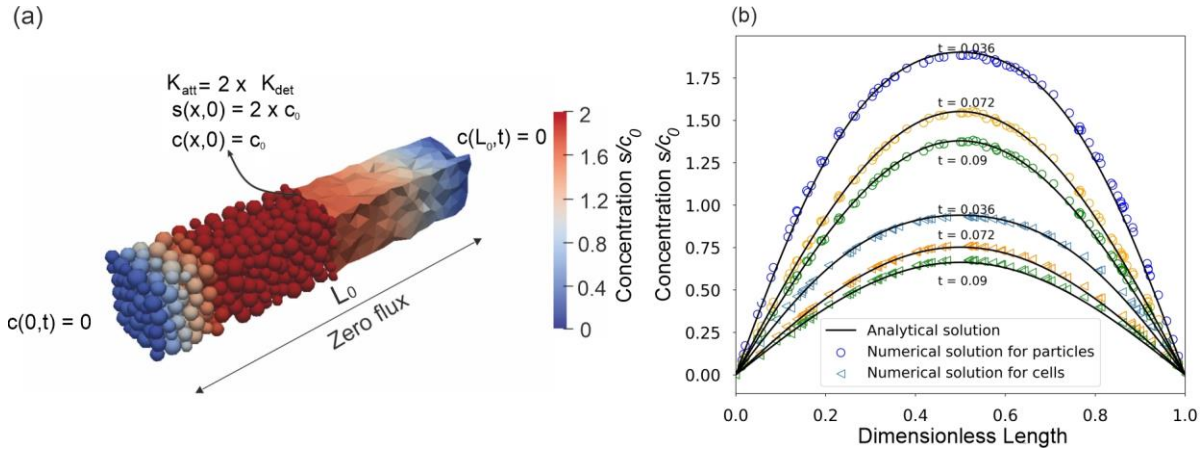

Figure 7. a) Concentration distribution in particles and pores simulated numerically at $t = 0.04$. b) Comparison of numerical and analytical concentration profiles in pores and particles at different times.

5 Hydro-mechanical behavior: comparison with a swelling experiment

To verify the implementation and validity of our HM scheme (Section 2.3), we compared the predictions of our model to the experimental results of Day et al. (Day et al., 2008a) who performed a swelling experiment on a 30 x 10 x 10 mm block of coal under confined conditions. The CO_2-induced coal swelling was measured for different values of CO_2 pressure by optical method. The experiment performed at 55°C on the Australian bituminous coal from the Bowen Basin (referred to as sample 3 in Day et al. (Day et al., 2008a) and as Qld8 in Day et al. (Day et al., 2008b)) was used as reference. Note that the same data set (but at 40°C) was also used by (Sampath et al., 2020) for model validation purpose but some discrepancies exist between our two investigations. Indeed, due to the lack of experimental data available, a part of their numerical properties were obtained from another coal experiment and they discarded the highest pressures of swelling experiment (higher than 12MPa) for comparison. In the present analysis, we did our best to carry out a fair comparison by using the full range of experimental data available and a complete set of consistent physical properties for this coal. All the parameter values are gathered in Table 2. Because the elastic properties and Biot coefficient were not provided either in (Day et al., 2008b, 2008a), we set the value of b based on the value used by Sampath et al. (Sampath et al., 2020). The Young modulus E and the Poisson ratio υ were chosen in order to reproduce the behavior observed by Day et al. (Day et al., 2008a) with a non-sorbing gas (a volumetric contraction of 0.06% was reached at 15MPa of helium pressure). The s_{max}

value was inferred from the maximum sorption capacity of the coal W_0 in the isotherm model calculated by Day et al. (Day et al., 2008b) (68.4 kg of CO_2 per ton of rock for the sample Qld 8). Finally, values of D^K and D^S were taken from the literature (Dong et al., 2017) whereas K_{att}, K_{det} were fixed arbitrarily. D^S is fixed constant but D^K varies as a function of the pore radius, as expressed in Equation (10), around an average value found in the literature (see Table 2). Note that the values chosen for these transport and kinetic parameters do not affect the steady-state behavior and hence, the comparison we made which is based on equilibrium states.

5.1 Sample preparation

A 10 x 10 x 10 mm particle assembly made up of 10,000 particles was generated and the interparticle properties calibrated following the approach proposed by Scholtès and Donzé (Scholtès and Donzé, 2013). The coal sample is considered isotropic although, even for the matrix, this assumption may be questioned (Day et al., 2008a). The calibration was done by performing uniaxial compression tests on the numerical sample following a trial and errors approach to determine the adequate interparticle properties to match both Young modulus and Poisson ratio of the coal. In addition, both the porosity and Biot coefficient of the numerical sample were defined to match those of the tested coal by following the procedures presented in Section 3.1.

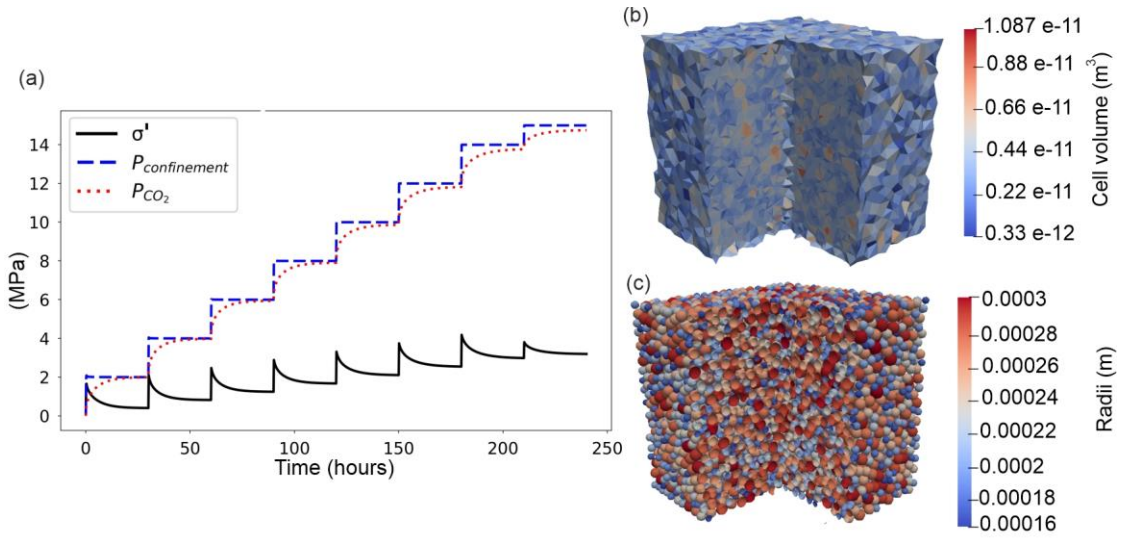

Figure 8 Numerical set up for simulating the swelling experiment of Day et al. (2008): a) boundary pressures and resulting mean effective stress, b) pore size distribution, c) particles size distribution.

480 Table 2

481 Numerical parameters used to simulate the coal matrix experiment by Day et al. [57]. The star symbol denotes
482 the calibration parameters.

Parameters	DEM-PFV model	Sources
Young modulus E (GPa) *	4.550	*computed from Day et al., 2008* (Day et al., 2008a) *(sample 3)*
Poisson ratio υ (-)*	0.225	*computed from Day et al., 2008* (Day et al., 2008a) *(sample 3)*
Temperature T (K)	328	*Day et al., 2008* (Day et al., 2008a) *(sample 3)*
Gas constant R (J.mol^{-1}.K^{-1})	8.314	*N/A*
Molar mass M_g (g.mol^{-1})	44.01	*N/A*
Bulk density (kg.m^{-3})	1220	*Day et al., 2008* (Day et al., 2008b) *(sample Qld 8, Table 3)*
Skeletal density (kg.m^{-3})	1303	*Day et al., 2008* (Day et al., 2008b) *(sample Qld 8, Table 3)*
s_{max} (mol.m^{-3})	2025	*Day et al., 2008* (Day et al., 2008b) *(sample Qld 8, Table 2)*
K_d (mol.m^{-3}) *	0.0017	-
K_{att} (s^{-1})	17e-11	-
K_{det} (mol.m^{-3}. s^{-1})	1e-7	-
D^K(×10^{-12} m^2.s^{-1})	3	*Dong et al., 2017* (Dong et al., 2017) *(Table 4)*
D^s(×10^{-12} m^2.s^{-1})	30	*Dong et al., 2017* (Dong et al., 2017) *(Table 4)*
Biot coefficient b (-)	0.8	*Sampath et al., 2020* (Sampath et al., 2020) *(Table 2)*
Coupling coefficient α (-) *	20.2	-
Porosity of assembly n_a (%)	32	*N/A*
Porosity of coal sample n_m (%)	7.1	*Day et al., 2008* (Day et al., 2008b) *(sample Qld 8, Table 3)*

483 *5.2 Experimental procedure*

484 Day et al. (Day et al., 2008a) measured the dimensional changes of a sample contained within a pressure cell
485 where CO_2 pressure was increased up to 15 MPa. In our experiment, the numerical sample is confined in between
486 6 frictionless boundary walls to control the confining pressure $p_{confinement}$. To reproduce the swelling experiment
487 of Day et al. (Day et al., 2008a), we imposed CO_2 pressure both as boundary stress ($p_{confinement}$) and as boundary
488 pressure (p_{CO2}) on all the sample boundaries. $p_{confinement}$ is adjusted by displacing the boundary walls. During
489 the simulation, p_{CO2} and $p_{confinement}$ were increased stepwise from equilibrium states and the volumetric
490 deformation ε_v, solvation pressure (p_s), adsorbed amount of gas (s) and fluid pressure (p_f) were recorded at each
491 step (Figure 8a).

492 Since the Biot coefficient is lower than one, the effective stress varies at each CO_2 injection pressure step. Day et
493 al. (Day et al., 2008a) however suggest that the mechanical compression caused by the pore pressure increase can

be neglected (0.06% of contraction for non-sorbing gas against 2% of swelling deformation with CO_2 at 15Mpa). In other words, Day et al. investigated throughout this experiment the influence of sorption-induced swelling on the poromechanical behavior of the material without taking into consideration the effect of the fluid bulk pressure.

5.3 Parametric study

Before directly comparing the model results with the experimental observations, a parametric study is presented to highlight the influence of the model parameters on the emergent behavior. The results are summarized in Figure 9 and the parameters roles assessed as follows:

- The coupling term α controls the intensity of the solvation pressure p_s (Equation (30), Figure 9b), hence the amplitude of the associated deformation (Equation (35), Figure 9c). Thus, α needs to be adjusted as a function of the swelling potential of the material with respect to the nature of the adsorbed fluid as, for example, CO2 induces larger swelling than CH_4 in coal (Durucan et al., 2009). p_s is directly proportional to α (Figure 9b), giving the opportunity to set its value so as to match experimental evidence of swelling for each combination of material and adsorbed fluid. One has to note that α does not influence the amount of molecules that can be adsorbed on the solid phase (Figure 9a).
- According to Equations (15) and (16), s_{max} determines the maximum amount of gas molecules that can be adsorbed on the surfaces of the solid phase. Depending on the nature of the fluid-solid interaction at play, s_{max} must be adjusted because it also affects the solvation pressure and thus the volumetric deformation (Figure 9d-e-f). In contrast, K_d controls the adsorption/desorption kinetics (Figure 9g-h-i) without influencing the maximum amount of adsorbed gas molecules, hence leading to the same plateau value for the adsorbed amount of gas molecules, solvation pressure and volumetric deformation.
- Finally, the Biot coefficient b does not influence neither the amount of adsorbed gas molecules nor the solvation pressure (Figure 9j-k) while it directly influences the volumetric deformation (Figure 9l), as described by the poromechanical equation (Equation (35)).

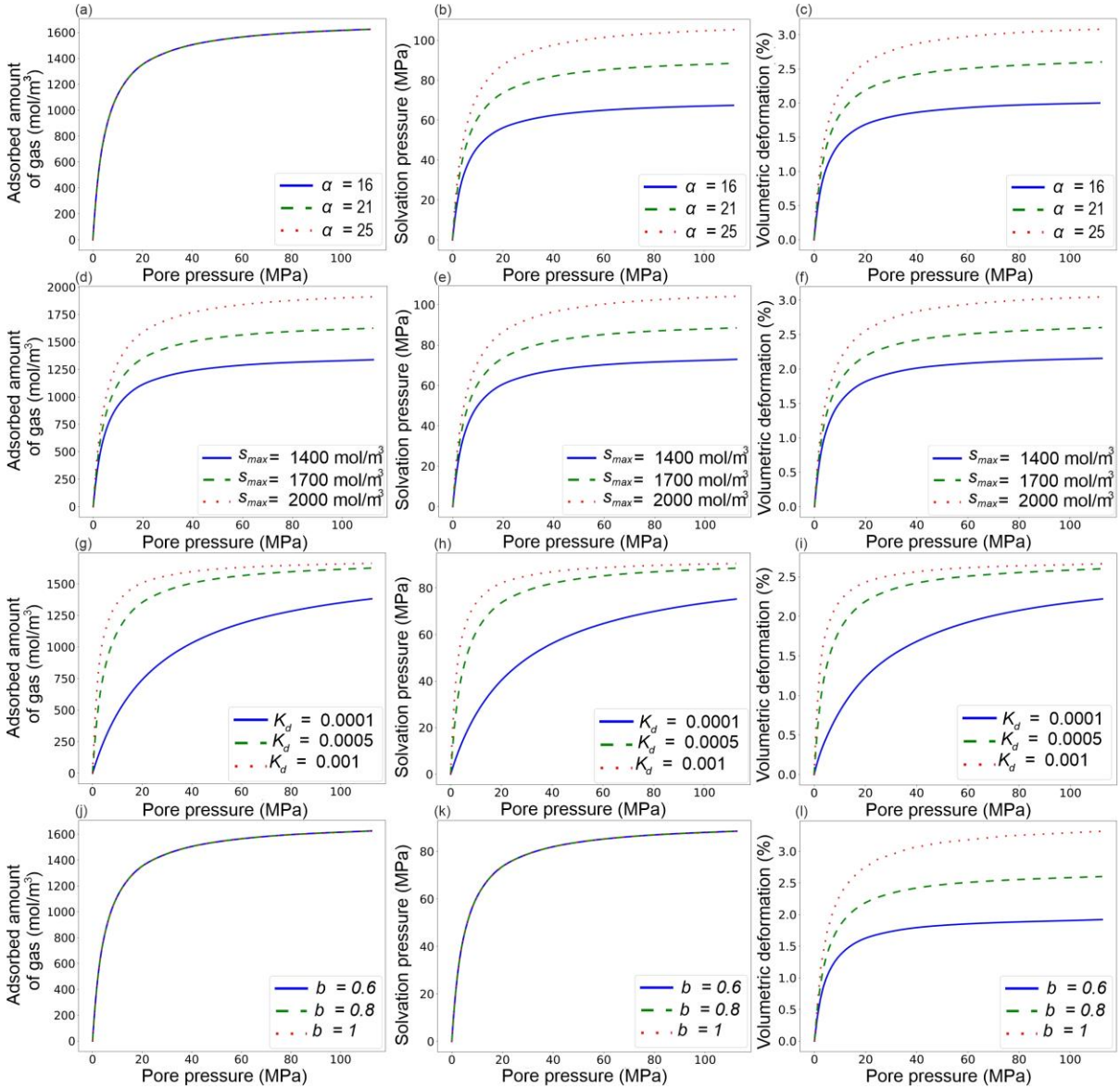

Figure 9 Evolution of adsorbed amount of gas s (left), solvation pressure p_s (middle) and volumetric deformation ε_v (right) versus pore pressure p_f for: (a,b,c) different α values and fixed parameters (s_{max}=1700, K_d=0.0005, b=0.8), (d,e,f) different s_{max} values and fixed parameters (α =21, K_d=0.0005, b=0.8), (g,h,i) different K_d values and fixed parameters (α =21, s_{max}=1700, b=0.8), (j.k,l) different b values and fixed parameters (α =21, K_d=0.0005, s_{max}=1700).

5.4 *Calibration procedure and comparison to the experiment of Day et al.*

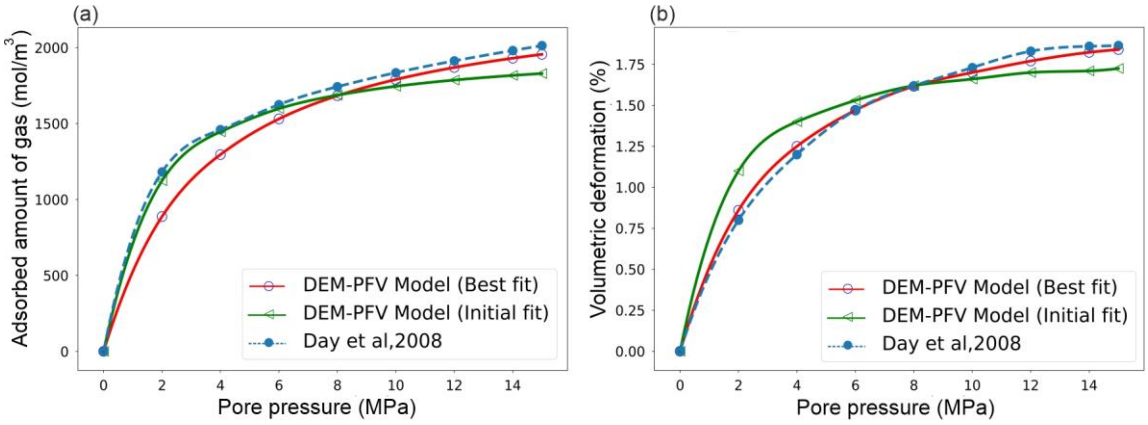

Figure 10 Swelling experiment: comparison of the DEM-PFV model predictions to the experiment of Day et al. (Day et al., 2008a): evolutions of a) adsorbed amount of gas and, b) volumetric deformation as functions of the pore pressure.

The calibration of the model was done through the following procedure:

1. Determine the interparticle elastic properties (E_{eq} and P) through uniaxial or triaxial compression testing (trial and error adjustments) to match both Young modulus E and Poisson ratio υ of the material.
2. Set b equal to the measured value and scale the numerical sample connected porosity $n_{a,c}$.
3. Determine the experimental solvation pressure p_S by using the extended poromechanical equations, (Equations (35) and (36)) such that

$$p_S = \frac{K\,\varepsilon_v + (\sigma - b p_f)}{b} \tag{47}$$

where $K = \frac{E}{3(1-2\vartheta)}$ is the bulk modulus and $\sigma = \frac{\sigma_{kk}}{3}$ is the mean stress and, from the value of s_{max}, estimate α using the plateau value of p_S.

4. Finally, calibrate K_d (trial and error adjustments) so that the numerical results fit with the experiments in terms of solvation pressure or swelling deformation.

The numerical results presented in Figure 10 (referred to as the initial fit) match the experimental observations for the following set of parameters: $\alpha = 20.02$, K_d = 0.0017 mol.m^{-3} with the s_{max} value inferred from the experiment (s_{max}= 2025 mol.m^{-3}). The fit to experimental data point is not ideal yet. In their study, Day et al. (Day et al., 2008b) have explored a pore filling isotherm model (Dubinin–Radushkevich model) which has been found to provide a better fit to experimental adsorption data than the classical Langmuir model, especially at high

pressures, above 6 MPa. A comparison between this isotherm model and ours is shown in Figure 10a and confirms this observation. This discrepancy, inherent to the use of Langmuir isotherm model, is also observed when comparing volumetric deformations in Figure 10b (an average error of 19% is found). Note that a better fit can be achieved when fitting also the s_{max} value. A second simulation, referred to as the best fit, where s_{max} = 2400 mol.m^{-3}, K_d = 0.0008 mol.m^{-3} and $\alpha = 20.02$ are shown in Figure 10a and Figure 10b. The error is thus reduced to 2%.

Additional insights can be gained from numerical simulations into the dynamics of mass transfer processes within the coal material. Figure 11 shows the changes in averaged gas and sorbed concentrations with time in the porous sample between two successive constant pressure steps. The corresponding porosity variation is also exhibited. As an illustrative example, we focused on the transient behavior corresponding to an increase from 0 to 15 MPa of CO_2 pressure. Results indicate that the gas diffuses first through the solid phase. As expected from diffusion values of Table 2 and accordingly to the literature (Dong et al., 2017; Mathias et al., 2020), surface diffusion is the predominant transport mechanism within coal matrix. This increase in sorbed concentration within the coal sample results in swelling and hence, volumetric strain and porosity increase. Owing to the values used for K_{att} and K_{det}, the desorption rate is not large enough and equilibrium is reached faster in the solid phase than in the gas phase (Figure 11). As a consequence, swelling occurs before the pore pressure reaches its equilibrium state in agreement with Sampath et al. results (Sampath et al., 2020).

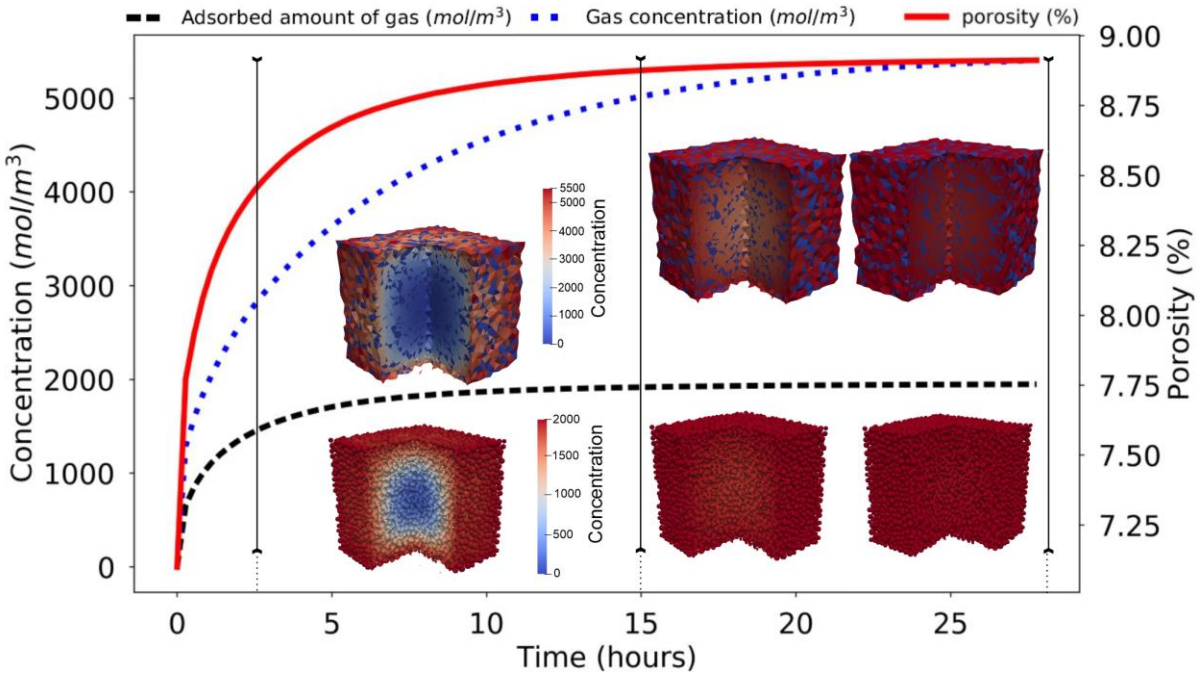

Figure 11. Evolution of porosity, fluid concentration and adsorbed amount of gas with time.

6 Conclusion

A new 3D pore-scale model for porous swelling materials is proposed to investigate coalbed methane production. In our model, a DEM model where the material is represented as an assembly of particles interacting one with another according to predefined contact laws is coupled to a PNM approach for describing transport mechanisms between and within pores and solid grains. The material is assumed to be saturated with gas and various mechanisms for gas transport across the coal matrix have been considered including Knudsen diffusion, surface diffusion and sorption. Mechanical couplings inherent to such swelling materials are also taken into account. The model simulates both (i) the interplay between pore pressure and external stress with variations in the effective stress which may impact the mechanical behavior of the medium and (ii) the sorption processes which contribute to swell or shrink the material. This latter mechanism is considered through the addition of an additional pressure term, classically called the solvation pressure, related to the sorbed concentration.

The implementation of the model was tested against analytical solutions and compared to a swelling experiment. The model was found to be robust and a suitable tool for describing adsorption induced deformation. This comprehensive investigation reveals the complex physics at stake during methane adsorption and the numerical results give precious insights onto the internal dynamics of gas within the coal matrix. In particular, simulations reveal that coal matrix swelling occurs before the pore pressure reaches its equilibrium state since surface diffusion prevails. The present model is thus capable to describe the strong coupling between transport, chemical (sorption) and mechanical processes and can be used to predict methane recovery. Future work will focus on introducing cleat network to assess the effect of cleat intensity and facilitate more comprehensive analysis on the permeability changes at the coal rock mass scale.

Acknowledgments: This study was conducted in the framework of a research and development project, Regalor (Ressources Gazières de Lorraine), carried by GeoRessources laboratory (Université de Lorraine— CNRS) on Grand-Est region‘s initiative and supported by the European Regional Development Fund.

7 References

Bertrand, F., Cerfontaine, B., Collin, F., 2017. A fully coupled hydro-mechanical model for the modeling of coalbed methane recovery. J. Nat. Gas Sci. Eng. 46, 307–325. https://doi.org/10.1016/j.jngse.2017.07.029

Biot, M.A., 1941. General Theory of Three-Dimensional Consolidation. J. Appl. Phys. 12, 155–164. https://doi.org/10.1063/1.1712886

Brochard, L., Vandamme, M., Pellenq, R.J.-M., 2012. Poromechanics of microporous media. J. Mech. Phys. Solids 60, 606–622. https://doi.org/10.1016/j.jmps.2012.01.001

Catalano, E., Chareyre, B., Barthélémy, E., 2014. Pore-scale modeling of fluid-particles interaction and emerging poromechanical effects. Int. J. Numer. Anal. Methods Geomech. 38, 51–71. https://doi.org/10.1002/nag.2198

Caulk, R., Scholtès, L., Krzaczek, M., Chareyre, B., 2020. A pore-scale thermo–hydro-mechanical model for particulate systems. Comput. Methods Appl. Mech. Eng. 372, 113292. https://doi.org/10.1016/j.cma.2020.113292

Ceglarska-Stefańska, G., Czapliński, A., 1993. Correlation between sorption and dilatometric processes in hard coals. Fuel 72, 413–417. https://doi.org/10.1016/0016-2361(93)90064-9

Ceglarska-Stefańska, G., Zarębska, K., 2002. The competitive sorption of CO2 and CH4 with regard to the release of methane from coal. Fuel Process. Technol. 77–78, 423–429. https://doi.org/10.1016/S0378-3820(02)00093-0

Chareyre, B., Cortis, A., Catalano, E., Barthélemy, E., 2012. Pore-Scale Modeling of Viscous Flow and Induced Forces in Dense Sphere Packings. Transp. Porous Media 94, 595–615. https://doi.org/10.1007/s11242-012-0057-2

Choi, J.-G., Do, D.D., Do, H.D., 2001. Surface Diffusion of Adsorbed Molecules in Porous Media: Monolayer, Multilayer, and Capillary Condensation Regimes. Ind. Eng. Chem. Res. 40, 4005–4031. https://doi.org/10.1021/ie010195z

Connell, L.D., 2016. A new interpretation of the response of coal permeability to changes in pore pressure, stress and matrix shrinkage. Int. J. Coal Geol. 162, 169–182. https://doi.org/10.1016/j.coal.2016.06.012

Cundall, P.A., Strack, O.D.L., 1979. A discrete numerical model for granular assemblies. Géotechnique 29, 47–65. https://doi.org/10.1680/geot.1979.29.1.47

Day, S., Duffy, G., Sakurovs, R., Weir, S., 2008b. Effect of coal properties on CO2 sorption capacity under supercritical conditions. Int. J. Greenh. Gas Control, EGU General Assembly 2007: Advances in CO2 Storage in Geological Systems 2, 342–352. https://doi.org/10.1016/S1750-5836(07)00120-X

Day, S., Fry, R., Sakurovs, R., 2008a. Swelling of Australian coals in supercritical CO2. Int. J. Coal Geol. 74, 41–52. https://doi.org/10.1016/j.coal.2007.09.006

Detournay, E., Cheng, A.H.-D., 1993. 5 - Fundamentals of Poroelasticity, in: Fairhurst, C. (Ed.), Analysis and Design Methods. Pergamon, Oxford, pp. 113–171. https://doi.org/10.1016/B978-0-08-040615-2.50011-3

Dilatation of Porous Glass - SCHERER - 1986 - Journal of the American Ceramic Society - Wiley Online Library [WWW Document], n.d. URL https://ceramics.onlinelibrary.wiley.com/doi/abs/10.1111/j.1151-2916.1986.tb07448.x (accessed 11.14.22).

Do, D.D., 1998. Adsorption Analysis: Equilibria And Kinetics (With Cd Containing Computer Matlab Programs). World Scientific.

Dolino, G., Bellet, D., Faivre, C., 1996. Adsorption strains in porous silicon. Phys. Rev. B 54, 17919–17929. https://doi.org/10.1103/PhysRevB.54.17919

Dong, J., Cheng, Y., Liu, Q., Zhang, H., Zhang, K., Hu, B., 2017. Apparent and True Diffusion Coefficients of Methane in Coal and Their Relationships with Methane Desorption Capacity. Energy Fuels 31, 2643–2651. https://doi.org/10.1021/acs.energyfuels.6b03214

Duriez, J., Scholtès, L., Donzé, F.-V., 2016. Micromechanics of wing crack propagation for different flaw properties. Eng. Fract. Mech. 153, 378–398. https://doi.org/10.1016/j.engfracmech.2015.12.034

Durucan, S., Ahsanb, M., Shia, J.-Q., 2009. Matrix shrinkage and swelling characteristics of European coals. Energy Procedia, Greenhouse Gas Control Technologies 9 1, 3055–3062. https://doi.org/10.1016/j.egypro.2009.02.084

Espinoza, D.N., Vandamme, M., Dangla, P., Pereira, J.-M., Vidal-Gilbert, S., 2013. A transverse isotropic model for microporous solids: Application to coal matrix adsorption and swelling. J. Geophys. Res. Solid Earth 118, 6113–6123. https://doi.org/10.1002/2013JB010337

642 Espinoza, D.N., Vandamme, M., Pereira, J.-M., Dangla, P., Vidal-Gilbert, S., 2014. Measurement and modeling
643 of adsorptive–poromechanical properties of bituminous coal cores exposed to CO2: Adsorption,
644 swelling strains, swelling stresses and impact on fracture permeability. Int. J. Coal Geol. 134–135, 80–
645 95. https://doi.org/10.1016/j.coal.2014.09.010
646 Gor, G.Yu., Neimark, A.V., 2010. Adsorption-Induced Deformation of Mesoporous Solids. Langmuir 26,
647 13021–13027. https://doi.org/10.1021/la1019247
648 Grosman, A., Ortega, C., 2008. Influence of elastic deformation of porous materials in adsorption-desorption
649 process: A thermodynamic approach. Phys. Rev. B 78, 085433.
650 https://doi.org/10.1103/PhysRevB.78.085433
651 Guo, X., Wang, Z., Zhao, Y., 2016. A comprehensive model for the prediction of coal swelling induced by
652 methane and carbon dioxide adsorption. J. Nat. Gas Sci. Eng. 36, 563–572.
653 https://doi.org/10.1016/j.jngse.2016.10.052
654 Jing, Y., Armstrong, R.T., Ramandi, H.L., Mostaghimi, P., 2017. Topological Characterization of Fractured
655 Coal. J. Geophys. Res. Solid Earth 122, 9849–9861. https://doi.org/10.1002/2017JB014667
656 Kowalczyk, P., Ciach, A., Neimark, A.V., 2008. Adsorption-Induced Deformation of Microporous Carbons:
657 Pore Size Distribution Effect. Langmuir 24, 6603–6608. https://doi.org/10.1021/la800406c
658 Laubach, S.E., Marrett, R.A., Olson, J.E., Scott, A.R., 1998. Characteristics and origins of coal cleat: A review.
659 Int. J. Coal Geol. 35, 175–207. https://doi.org/10.1016/S0166-5162(97)00012-8
660 Li, Z., Liu, D., Cai, Y., Ranjith, P.G., Yao, Y., 2017. Multi-scale quantitative characterization of 3-D pore-
661 fracture networks in bituminous and anthracite coals using FIB-SEM tomography and X-ray μ-CT.
662 Fuel 209, 43–53. https://doi.org/10.1016/j.fuel.2017.07.088
663 Liu, J., Chen, Z., Elsworth, D., Qu, H., Chen, D., 2011. Interactions of multiple processes during CBM
664 extraction: A critical review. Int. J. Coal Geol. 87, 175–189. https://doi.org/10.1016/j.coal.2011.06.004
665 Liu, L., Luo, X.-B., Ding, L., Luo, S.-L., 2019. 4 - Application of Nanotechnology in the Removal of Heavy
666 Metal From Water, in: Luo, X., Deng, F. (Eds.), Nanomaterials for the Removal of Pollutants and
667 Resource Reutilization, Micro and Nano Technologies. Elsevier, pp. 83–147.
668 https://doi.org/10.1016/B978-0-12-814837-2.00004-4
669 Liu, M., Mostaghimi, P., 2017. Pore-scale modelling of CO2 storage in fractured coal. Int. J. Greenh. Gas
670 Control 66, 246–253. https://doi.org/10.1016/j.ijggc.2017.09.007
671 Ma, T., Rutqvist, J., Oldenburg, C.M., Liu, W., 2017. Coupled thermal–hydrological–mechanical modeling of
672 CO2-enhanced coalbed methane recovery. Int. J. Coal Geol. 179, 81–91.
673 https://doi.org/10.1016/j.coal.2017.05.013
674 Majewska, Z., Majewski, S., Ziętek, J., 2010. Swelling of coal induced by cyclic sorption/desorption of gas:
675 Experimental observations indicating changes in coal structure due to sorption of CO2 and CH4. Int. J.
676 Coal Geol. 83, 475–483. https://doi.org/10.1016/j.coal.2010.07.001
677 Mathias, S.A., Dentz, M., Liu, Q., 2020. Gas Diffusion in Coal Powders is a Multi-rate Process. Transp. Porous
678 Media 131, 1037–1051. https://doi.org/10.1007/s11242-019-01376-x
679 Mostaghimi, P., Armstrong, R.T., Gerami, A., Hu, Y., Jing, Y., Kamali, F., Liu, M., Liu, Z., Lu, X., Ramandi,
680 H.L., Zamani, A., Zhang, Y., 2017. Cleat-scale characterisation of coal: An overview. J. Nat. Gas Sci.
681 Eng. 39, 143–160. https://doi.org/10.1016/j.jngse.2017.01.025
682 Mostaghimi, P., Armstrong, R.T., Gerami, A., Hu, Y., Jing, Y., Kamali, F., Liu, M., Liu, Z., Lu, X., Ramandi,
683 H.L., Zamani, A., Zhang, Y., 2016. Pore Scale Characterisation of Coal: An Unconventional
684 Challenge. Presented at the Abu Dhabi International Petroleum Exhibition & Conference, OnePetro.
685 https://doi.org/10.2118/183411-MS
686 Mushrif, S.H., Rey, A.D., 2009. An integrated model for adsorption-induced strain in microporous solids.
687 Chem. Eng. Sci., Morton Denn Festschrift 64, 4744–4753. https://doi.org/10.1016/j.ces.2009.04.014
688 Nikoosokhan, S., Vandamme, M., Dangla, P., 2014. A poromechanical model for coal seams saturated with
689 binary mixtures of CH4 and CO2. J. Mech. Phys. Solids 71, 97–111.
690 https://doi.org/10.1016/j.jmps.2014.07.002
691 Ottiger, S., Pini, R., Storti, G., Mazzotti, M., 2008. Competitive adsorption equilibria of CO2 and CH4 on a dry
692 coal. Adsorption 14, 539–556. https://doi.org/10.1007/s10450-008-9114-0
693 Pan, Z., Connell, L.D., 2007. A theoretical model for gas adsorption-induced coal swelling. Int. J. Coal Geol.
694 69, 243–252. https://doi.org/10.1016/j.coal.2006.04.006
695 Papachristos, E., Scholtès, L., Donzé, F.V., Chareyre, B., 2017. Intensity and volumetric characterizations of
696 hydraulically driven fractures by hydro-mechanical simulations. Int. J. Rock Mech. Min. Sci. 93, 163–
697 178. https://doi.org/10.1016/j.ijrmms.2017.01.011

Perrier, L., Pijaudier-Cabot, G., Grégoire, D., 2018. Extended poromechanics for adsorption-induced swelling prediction in double porosity media: Modeling and experimental validation on activated carbon. Int. J. Solids Struct. 146, 192–202. https://doi.org/10.1016/j.ijsolstr.2018.03.029
Pijaudier-Cabot, G., Vermorel, R., Miqueu, C., Mendiboure, B., 2011. Revisiting poromechanics in the context of microporous materials. Comptes Rendus Mécanique 339, 770–778. https://doi.org/10.1016/j.crme.2011.09.003
Pini, R., Ottiger, S., Burlini, L., Storti, G., Mazzotti, M., 2009. Role of adsorption and swelling on the dynamics of gas injection in coal. J. Geophys. Res. Solid Earth 114. https://doi.org/10.1029/2008JB005961
Privalov, V., Pironon, J., de Donato, P., Michels, R., Morlot, C., Izart, A., 2020. Natural Fracture Systems in CBM Reservoirs of the Lorraine–Saar Coal Basin from the Standpoint of X-ray Computer Tomography. Environ. Sci. Proc. 5, 12. https://doi.org/10.3390/IECG2020-08772
Raoof, A., Nick, H.M., Wolterbeek, T.K.T., Spiers, C.J., 2012. Pore-scale modeling of reactive transport in wellbore cement under CO2 storage conditions. Int. J. Greenh. Gas Control, CATO: CCS Research in the Netherlands 11, S67–S77. https://doi.org/10.1016/j.ijggc.2012.09.012
Reinecke, S.A., Sleep, B.E., 2002. Knudsen diffusion, gas permeability, and water content in an unconsolidated porous medium. Water Resour. Res. 38, 16-1-16–15. https://doi.org/10.1029/2002WR001278
Sampath, K.H.S.M., Perera, M.S.A., Matthai, S.K., Ranjith, P.G., Dong-yin, L., 2020. Modelling of fully-coupled CO2 diffusion and adsorption-induced coal matrix swelling. Fuel 262, 116486. https://doi.org/10.1016/j.fuel.2019.116486
Scholtès, L., Chareyre, B., Michallet, H., Catalano, E., Marzougui, D., 2015. Modeling wave-induced pore pressure and effective stress in a granular seabed. Contin. Mech. Thermodyn. 27, 305–323. https://doi.org/10.1007/s00161-014-0377-2
Scholtès, L., Donzé, F.-V., 2013. A DEM model for soft and hard rocks: Role of grain interlocking on strength. J. Mech. Phys. Solids 61, 352–369. https://doi.org/10.1016/j.jmps.2012.10.005
Šmilauer, V., Chareyre, B., Duriez, J., Eulitz, A., Gladky, A., Guo, N., Jakob, C., Kozicki, J., Kneib, F., Modenese, C., Stransky, J., Thoeni, K., 2015. Using and Programming. https://doi.org/10.5281/zenodo.34043
Thorstenson, D.C., Pollock, D.W., 1989. Gas transport in unsaturated zones: Multicomponent systems and the adequacy of Fick's laws. Water Resour. Res. 25, 477–507. https://doi.org/10.1029/WR025i003p00477
Ustinov, E.A., Do, D.D., 2006. Effect of adsorption deformation on thermodynamic characteristics of a fluid in slit pores at sub-critical conditions. Carbon 44, 2652–2663. https://doi.org/10.1016/j.carbon.2006.04.015
Vermorel, R., Pijaudier-Cabot, G., 2014. Enhanced continuum poromechanics to account for adsorption induced swelling of saturated isotropic microporous materials. Eur. J. Mech. - ASolids 44, 148–156. https://doi.org/10.1016/j.euromechsol.2013.10.010
Wang, S., Elsworth, D., Liu, J., 2011. Permeability evolution in fractured coal: The roles of fracture geometry and water-content. Int. J. Coal Geol. 87, 13–25. https://doi.org/10.1016/j.coal.2011.04.009
Wang, Z., Cheng, Y., Zhang, K., Hao, C., Wang, L., Li, W., Hu, B., 2018. Characteristics of microscopic pore structure and fractal dimension of bituminous coal by cyclic gas adsorption/desorption: An experimental study. Fuel 232, 495–505. https://doi.org/10.1016/j.fuel.2018.06.004
Wu, Y., Liu, J., Elsworth, D., Chen, Z., Connell, L., Pan, Z., 2010. Dual poroelastic response of a coal seam to CO2 injection. Int. J. Greenh. Gas Control 4, 668–678. https://doi.org/10.1016/j.ijggc.2010.02.004
Yang, K., Lu, X., Lin, Y., Neimark, A.V., 2010. Deformation of Coal Induced by Methane Adsorption at Geological Conditions. Energy Fuels 24, 5955–5964. https://doi.org/10.1021/ef100769x
Youjun, J., Vafai, K., 2017. Analysis of pore scale fluid migration in a porous medium - application to coal rock seam. Int. J. Numer. Methods Heat Fluid Flow 27, 1706–1719. https://doi.org/10.1108/HFF-05-2016-0198